Petroleum Science (2019) 16:14–31
https://doi.org/10.1007/s12182-018-0292-4

ORIGINAL PAPER

Tertiary hydrothermal activity and its effect on reservoir properties in the Xihu Depression, East China Sea

Yan Liu[1,2] · Si-Ding Jin[1,2] · Qian Cao[3] · Wen Zhou[1,2]

Received: 11 January 2018 / Published online: 3 January 2019
© The Author(s) 2019

Abstract

Three large-scale episodes of volcanic activity occurred during the Tertiary in the Xihu Depression, located in the East China Sea. Intermediate-felsic magmas intruded along faults and the associated hydrothermal fluids resulted in the hydrothermal alteration of the clastic country rock. To better describe reservoir characteristics, reservoir samples were subjected to the following investigations: thin section examination, scanning electron microscope-energy dispersive spectrometer analysis (SEM–EDS), fluid inclusion homogenization temperature tests, vitrinite reflectance measurements, and X-ray diffraction. The results of this study provide evidence of the following hydrothermal alteration phenomena: brittle fracturing, clastic particle alteration, precipitation of unique hydrothermal minerals (celestite, zircon, apatite, barite, and cerous phosphate). The presence of abnormally high temperatures is indicated by fluid inclusion analysis, the precipitation of high-temperature authigenic minerals such as quartz, illite alteration, and anomalous vitrinite reflectance. Two aspects related to hydrothermal effects on reservoir properties have been investigated in this study: (1) Deep magmatic hydrothermal fluids carry large amounts of dissolved carbon dioxide and sulfur dioxide gas. These fluids percolate into the country rocks along fault zones, resulting in dissolution within the sandstone reservoirs and the development of significant secondary porosity. (2) Magma intrusions increase the temperature of the surrounding rocks and accelerate the thermal evolution of hydrocarbon source rocks. This results in the release of large amounts of organic acids and carbon dioxide, leading the dissolution of the aluminosilicate minerals and volcanic fragments in the reservoirs, and the generation of significant secondary porosity.

Keywords Hydrothermal activities · Erosion effects · Clastic rock reservoir · Secondary porosity · Xihu Depression

1 Introduction

The term "hydrothermal fluids" refers to all high-temperature aqueous fluids (temperature range from 50 to 400 °C) that contain many chemical materials in solution (e.g., H_2S, HCl, HF, SO_2, CO, CO_2, H_2, N_2, KCl, and NaCl), some of which are highly reactive (Tao and Xu 1994). Hydrothermal fluids can originate from magmatic fluids, metamorphic fluids, hot brine and/or formation water in sedimentary basins, and fluids from primary mantle fluids (Chen et al. 2007). In this paper, the term "hydrothermal fluids" refers to magmatic hydrothermal fluids.

Magmatism occurs in many sedimentary basins around the world and has a significant impact on the generation, migration, and accumulation of oil and gas as well as the formation of hydrocarbon reservoirs due to the two following mechanisms (Ye et al. 2005; Agusto et al. 2013). (1) Thermal baking caused by the magmatic intrusion heats the surrounding rocks and results in mineral transformations. The thermal baking effect on hydrocarbon source rocks accelerates the generation of alkanes, organic acids, and carbon dioxide (Guo 2002). Girard and Nahon (1989) proposed the concept of "contact diagenesis," the "abnormally high temperatures" from the magmatic intrusion result in changes in the authigenic mineral assemblage in the contact zone. (2)

Edited by Jie Hao

✉ Si-Ding Jin
jinsiding@cdut.edu.cn

[1] State Key Laboratory of Oil and Gas Reservoir Geology and Exploitation, Chengdu University of Technology, Chengdu 610059, Sichuan, China

[2] College of Energy and Resources, Chengdu University of Technology, Chengdu 610059, Sichuan, China

[3] Sichuan Key Laboratory of Shale Gas Evaluation and Exploitation, Sichuan Keyuan Testing Center, Chengdu 610091, Sichuan, China

A series of water–rock reactions within the country rocks takes place as hydrothermal fluids move along migration pathways. This has a vital impact on reservoir performance.

Hydrothermal activity may result in the pores of reservoir rocks being filled with zeolite, calcite, chlorite, and siliceous minerals, which reduce the porosity and permeability of the country rocks to a considerable degree and therefore negatively impact the reservoir quality (Wang and Zhang 2001). In addition, researchers have suggested that hydrothermal fluids related to magmatic-volcanic activity are rich in CO_2, SO_2, and H_2S. The migration of these hydrothermal fluids along fault and fracture systems accelerates the thermal evolution of the hydrocarbon source rocks and released organic acids and CO_2 form a dissolution alteration zone (Hedenquist and Henley 1985; Yu et al. 2012; Liu et al. 2017; Wang et al. 2017a, b). For example, cyclic thermal convection in sedimentary basins on the western coast of Canada generated a dissolution zone of carbonate minerals and improved reservoir quality (Charlou et al. 2010; Schmidt et al. 2011). In the Pearl River Mouth Basin in China, magmatism not only caused relatively strong deformation and contact metamorphism but also provided a significant amount of heat, which resulted in abnormally high geothermal gradients accelerating the maturation of hydrocarbon source rocks and leading to the release of more organic acids, resulting in the development of secondary porosity (Nie et al. 2005; Zhu et al. 1994). Sugisaki and Mimura (1994) proposed that hydrothermal fluids rich in CO_2 underwent a chemical reaction with the reservoir rocks, causing the dissolution of quartz and feldspar particles which improves the reservoir properties of these rocks. Evidence for intrusive magmatic activity has been identified in different regions across the world during exploration for oil and gas, such as in the Michigan Basin in the United States (Wierzbicki et al. 2006), the Songliao Basin and the Jiyang Depression in eastern China (Wang et al. 1990), the offshore Bohai Bay Basin in Eastern China (Wang and Zhang 2001), the Dongpu Depression in eastern China (Zhu et al. 1994) and the offshore Yinggehai Basin in Southern China (Wang et al. 2010). In these basins, magmatic hydrothermal fluids have altered the reservoirs, and most of these altered reservoirs form a group of key hydrocarbon play pathways. Consequently, the impact of magmatic activity and associated magmatic hydrothermal fluids on petroleum systems has drawn a significant amount of research interest in the field of oil and gas exploration and development (Shu et al. 2003).

Exploration in the Xihu Depression, part of the continental shelf basin of the East China Sea has resulted in the discovery of considerable oil and gas reserves. The amount of oil and gas resources in the Xihu Depression is estimated to be more than 4.67 billion tonnes (Cao et al. 2017; Huang et al. 2010). Based on the analysis of temperature and thermal conductivity measurements taken in the Xihu Depression (with an average thermal flow of 71 mW/m^2), Wei et al. (1994) suggested that regional thermal anomalies were related to late-stage magmatic activity, fault development, hydrothermal activity, basement uplift and topography. The relatively frequent episodes of Tertiary magmatism in the central and southern parts of this area can be delineated in seismic profiles (Hu and Tao 1997), and most wells have encountered magmatic rocks (Zhou and Song 2014). Through analysis of the abnormally high porosity zones in the Paleogene of the Xihu Depression, Su et al. (2016) suggested that feldspar and other minerals had been eroded due to the action of organic acids and/or fluids, resulting in secondary porosity. Cao et al. (2017) indicated that the presence of abnormal overpressures inhibited compaction by overlying strata and increased the intensity of the dissolution effect, therefore resulting in the abnormally high porosities observed in the deep sandstone reservoirs.

To date, the effect of magmatic thermal fluids on reservoirs in the Xihu Depression has not been studied in detail. In the case of the Xihu depression, which is difficult to explore and develop and therefore has a high economic threshold, it is very important to clarify the controlling factors on high quality reservoirs in the context of the low porosity and low permeability observed in these deep reservoirs (> 3200 m). This research has led to a theoretical basis for the evaluation of deep, high quality reservoirs in the study area. In this paper, the authors investigated in detail evidence for deep hydrothermal processes and their effects on surrounding country rocks, documenting for the first time the influence of magmatic hydrothermal fluids on the reservoir properties of the country rocks.

The study focuses on the reservoirs of the Paleogene–Eocene Pinghu Formation and the Oligocene Huagang Formation in the Xihu Depression of the East China Sea. Cores from 14 wells in the southern part of the depression have been studied. A range of methods, including core and thin section examination, electron microprobe analysis, fluid inclusion analysis, and vitrinite reflectance, have been employed to investigate the samples' petrography and mineralogy to identify the presence and impact of magmatic hydrothermal fluids.

2 Geological setting

The Xihu Depression is within the continental shelf basin of the East China Sea located on China's eastern continental margin (Fig. 1). It is a tertiary oil and gas bearing depression in the northern part of the East Zhejiang Depression. Classed as a continental margin rift-depression basin it covers an area of 59,000 km^2. The boundary to the west is the Diaoyu Islands fold zone, and to the east are the Hupijiao, Haijiao, and Yushan Uplifts (Fig. 1). (Liu 1992; Xu et al.

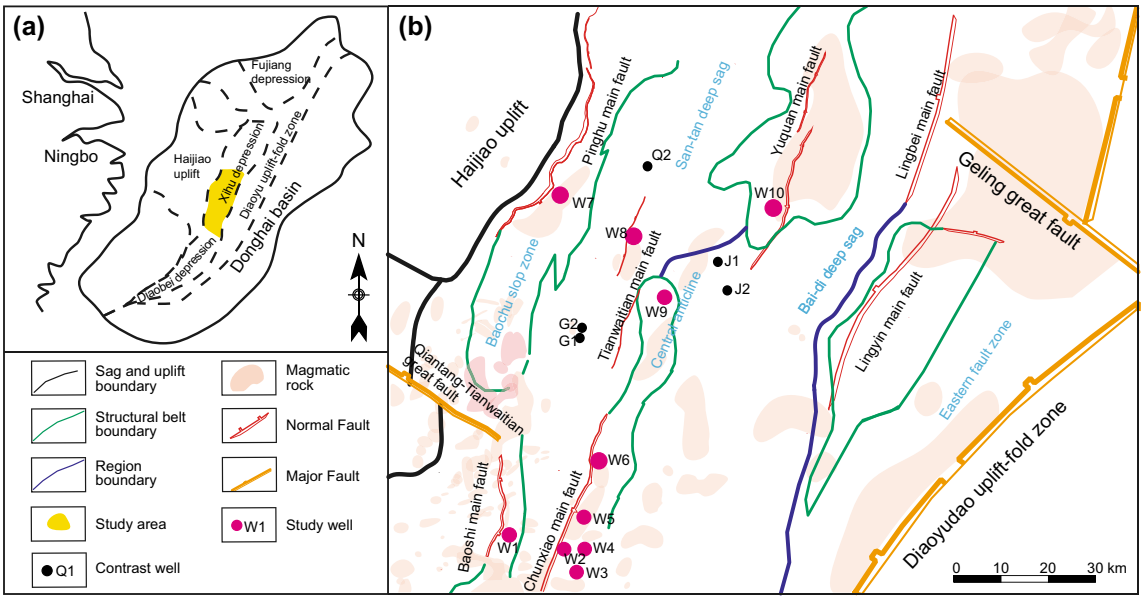

Fig. 1 Regional tectonic map and distribution of magmatic rocks of the Xihu Depression

1997; Liu et al. 2003). The structural framework shows NNE–NE, NW, and approximately E–W-trending fault zones that have undergone intense activity. The Xihu Depression can be divided into five tectonic units from west to east: The Baochu slope zone, the San-tan deep sag, the Central anticline, the Bai-di deep sag and the Eastern fault zone (Fig. 1).

Cenozoic clastic sediments developed in the Xihu Depression include (from bottom to top), the Paleocene (E_1), Eocene Baoshi Formation (E_2b), Pinghu Formation (E_2p), Oligocene Huagang Formation (E_3h), Miocene Longjing Formation (N_1^1l), Yuquan Formation (N_1^2y), Liulang Formation (N_1^3l), Pliocene Santan Formation (N_2s), and Quaternary East China Sea Formation (Qd) (Fig. 2). The Pinghu Formation depositional environment was a deltaic sedimentary system propagating into a restricted bay that was affected by tidal action. The Huagang Formation contains three sedimentary systems, namely lacustrine facies, braided river delta facies and fluvial facies. The reservoir lithology mainly consists of well-sorted feldspathic, lithic sandstones and lithic feldspathic sandstones with good sorting, and with rarer occurrence of lithic quartz sandstones and feldspathic quartz sandstones. On the basis of the analysis of the sedimentary environment, the strata can be characterized as layers of mudstone layers, silty mudstones and sandstones separated by andesites and basalts.

The Xihu Depression underwent a faulting stage, a local subsidence stage and a regional subsidence stage. (1) Faulting stage: The Keelung Movement resulted in initial rifting during the Late Cretaceous. Paleocene-Eocene sediments distributed across the entire Xihu Depression were cut by large basement faults, most of which were NE- and NNE-trending normal faults. The Oujiang Movement was the main period of extensional rifting during the early Eocene (E_2). (2) The Local Subsidence stage comprises three tectonic episodes including: (a) The Yuquan Movement, the first reversal period during the early Oligocene, with compression, folding and uplift accompanied by magmatic activity, and the development of the boundary interface (T_3^0) between the faulting stage and the Local Subsidence stage. (b) The Huagang Movement, the second inversion period during the late Oligocene, resulting in folding related to reverse faulting, uplift and erosion. This inversion led to folding, uplift and exposure of the formations proximal to the fault zone. (c) The Longjing Movement; the third phase of inversion at the end of the Miocene, resulted in tectonic inversion of the Central Depression Belt characterized by folding, uplifting and erosion. (3) Regional Subsidence stage: The main period of subsidence began Pliocene (N_1). During the subsidence of the basin, the Neogene-Quaternary strata were deformed by E–W-trending tensile-shear faults, mainly located in the central tectonic zone and the slope of the Xihu Depression (Zhang 2013).

The main faults are strike-slip extensional normal faults and extensional faults with a dip angle of 60°–80° in the Xihu Depression. The main active time of the faulting was late Cretaceous–Oligocene. The distribution of magmatic rocks in the research area is clearly controlled by faults (Cai et al. 2014) (Fig. 1). The magmatic rocks are mostly distributed along deep NE–NNE-trending faults (Zhang et al. 2014). The age of the magmatism decreases gradually from west to east; this is consistent with the fault activity time that shows a decreasing trend from west to east, associated with

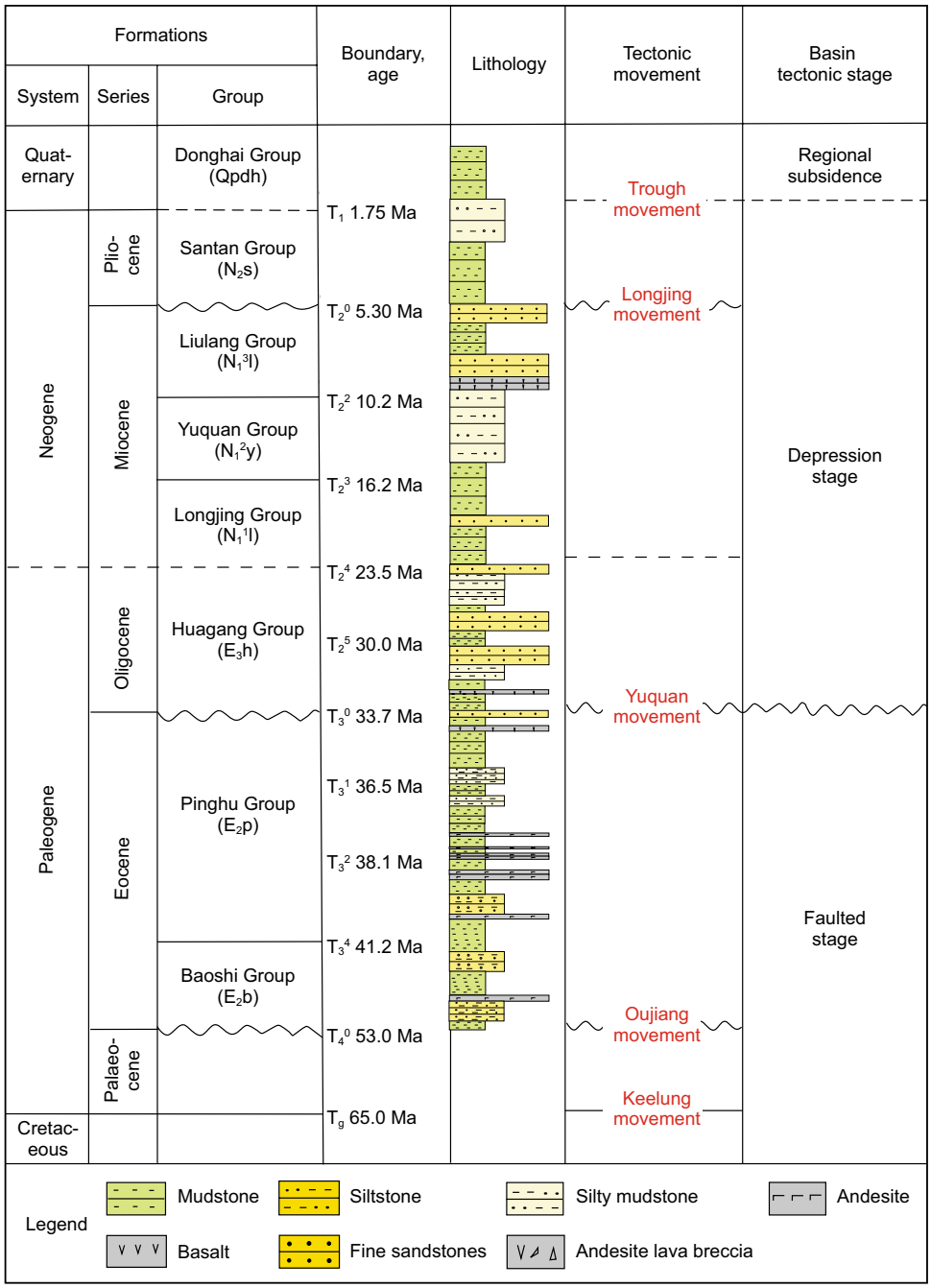

Fig. 2 The distribution of formation lithology in Xihu Depression

depositional center migration from west to east either (Hu and Tao 1997). Faulted regions are ideal pathways for the upward migration of deep fluids (Meng et al. 2008).

Based on seismic, gravity and magmatic data, geochemical data, and isotope chronology data (K–Ar and U–Pb methods), three episodes of Cenozoic volcanic activity have been identified by previous researchers. The activities include two kinds of intrusions and eruptions, forming intrusive rocks and volcanic rocks dominated by intermediate acid rocks, including Early Eocene emplacement of intermediate-mafic igneous rocks, Late Oligocene emplacement of intermediate-felsic magmatic rocks, and emplacement of Miocene magmatic rocks (Shen et al. 2001) (Fig. 2, Table 1). In particular, the Late Oligocene intermediate-felsic magmatic rocks penetrate through the T_3^0 reflection layer (33.7 Ma) and intrude into individual seismic sequences in the form of dykes. The intense magmatic episode in the Miocene resulted in intrusions and magma flows along the T_2^0 group bedding surfaces.

Table 1 The distribution of magmatic rocks in wells

Well	Magmatic rock section, m	Horizon	Thickness, m	Rock types
W5	2809–3104	Huagang Formation (E_3h)	195	Andesite-dacites, basalt-andesite
	3104–3204.7	Pinghu Formation (E_2p)	100	Meta andesitic volcanic breccia
W6	4774–4847	Pinghu Formation (E_2p)	73	Andesite, diorite, tuff
	4895–4983	Pinghu Formation (E_2p)	22	Altered dacite
W7	3566–3685.5	Pinghu Formation (E_2p)	1.07	Andesite, basalt, andesitic tuff lava, tuff
	3840.5–4053.5	Pinghu Formation (E_2p)	265	Tuff breccia, granite, granodiorite
	4190–4240, 4262–4275	Pinghu Formation (E_2p)	63	Tuff
W8	1995–2012.5	Longjing Formation (N_1^1l)	17.5	Dacites cutting crystal tuff, dacites tuff breccia diorite, andesite, tuff
W9	2381–2560	Longjing Formation (N_1^1l)	47	Altered tuff
W10	2162.5–2167.9	Huagang Formation (E_3h)	5.4	Crystal tuff
G1	1995–2012.5	Yuquan Formation (N_1^2y)	17.5	Tuff

Sample data from Wei et al. (1994), Hu and Tao (1997), Zhou and Song (2014)

Based on observations of the successive precipitation of minerals in response to pressure and temperature changes, the diagenetic evolution sequence is determined as follows: mechanical compaction, early carbonate cementation, early dissolution (caused by water-soluble corrosion resulting in feldspar erosion to kaolinite), secondary enlargement of quartz, late carbonate cementation, late dissolution, iron and calcite and dolomite precipitation. The formation of secondary pores is mainly controlled by late cementation and dissolution. This late dissolution occurs in the middle diagenetic stages A-B that occurred in the Late Oligocene and Miocene, thus providing the link between burial history and hydrocarbon generation. Once the source rock passed through the hydrocarbon generation window, three subsequent pulses of hydrocarbon migration took place during the Early Miocene (25 Ma), Late Miocene (10.4–6.1 Ma) and Early Pliocene (2.2–0 Ma), (Fig. 3) (Cao 2016; Su et al. 2016). The late dissolution occurred prior to hydrocarbon charging.

Previous studies on the burial and thermal history of the Xihu Depression suggested that the thermal effects of magmatic intrusives were detectable in the southern part of the central uplift zone and the Sudi Structural Zone (Zhou 2003; Su et al. 2016). Correlating with pulses of magmatism in the Xihu Depression, three phases of magmatic hydrothermal activity could be identified: an Early Paleocene-Eocene event, a Late Oligocene event, and a Miocene event. Early and mid-term hydrothermal activity has had the greatest impact on hydrocarbon generation and expulsion from source rocks. The regional heat from the Early Paleocene-Eocene magmatism accelerated the thermal evolution of the source rocks. By the end of the Oligocene, large amounts of hydrocarbons and associated gas had been generated (Gu et al. 2001). Therefore, the mechanism of dissolution of alkaline minerals by CO_2-rich acidic fluids linked to the influence of magmatic hydrothermal fluids on the source rock thermal evolution has been discussed in this paper.

3 Methodology

Seventy-four core samples were collected from 10 wells in the Xihu Depression, well W1 in the Baoshi Fault Zone, wells W2–W6 in the Chunxiao Fault Zone, well W7 in the Pinghu Fault Zone, wells W8, W9 in the Tianwaitian Fault Zone and well W10 in the Yuquan main fault (Fig. 1). The samples were analyzed at the State Key Laboratory for Oil and Gas Reservoir Geology and Exploration at the Chengdu University of Technology. The following is an overview of the methods used in this investigation:

(1) A Nikon E600 microscope and a Wisesoft microscopic image analyzer were used to examine and study lithology and pore structures, magnification is 25–400 times.
(2) A CL8200 MK5 cathode luminescence microscope was used to determine the texture of quartz and feldspar debris, the growth zone of calcite cement, and the clay minerals. The voltage of the beam is 15 kV, and the beam current is 300 μA.
(3) A field-emission environmental scanning electron microscope (Quanta 250 FEG, manufactured by FEI, United States) with an energy-dispersive spectrometer (EDS) was used to conduct high-resolution morphological observations and analyses of rock samples in the ESEM™ vacuum environment. The EDS was used to characterize the structure and composition of the samples from their surface images and component images. The resolution of the electronic image is 1.0 nm @ 30 kV, 3.0 nm @1 kV, and the resolution of the back-

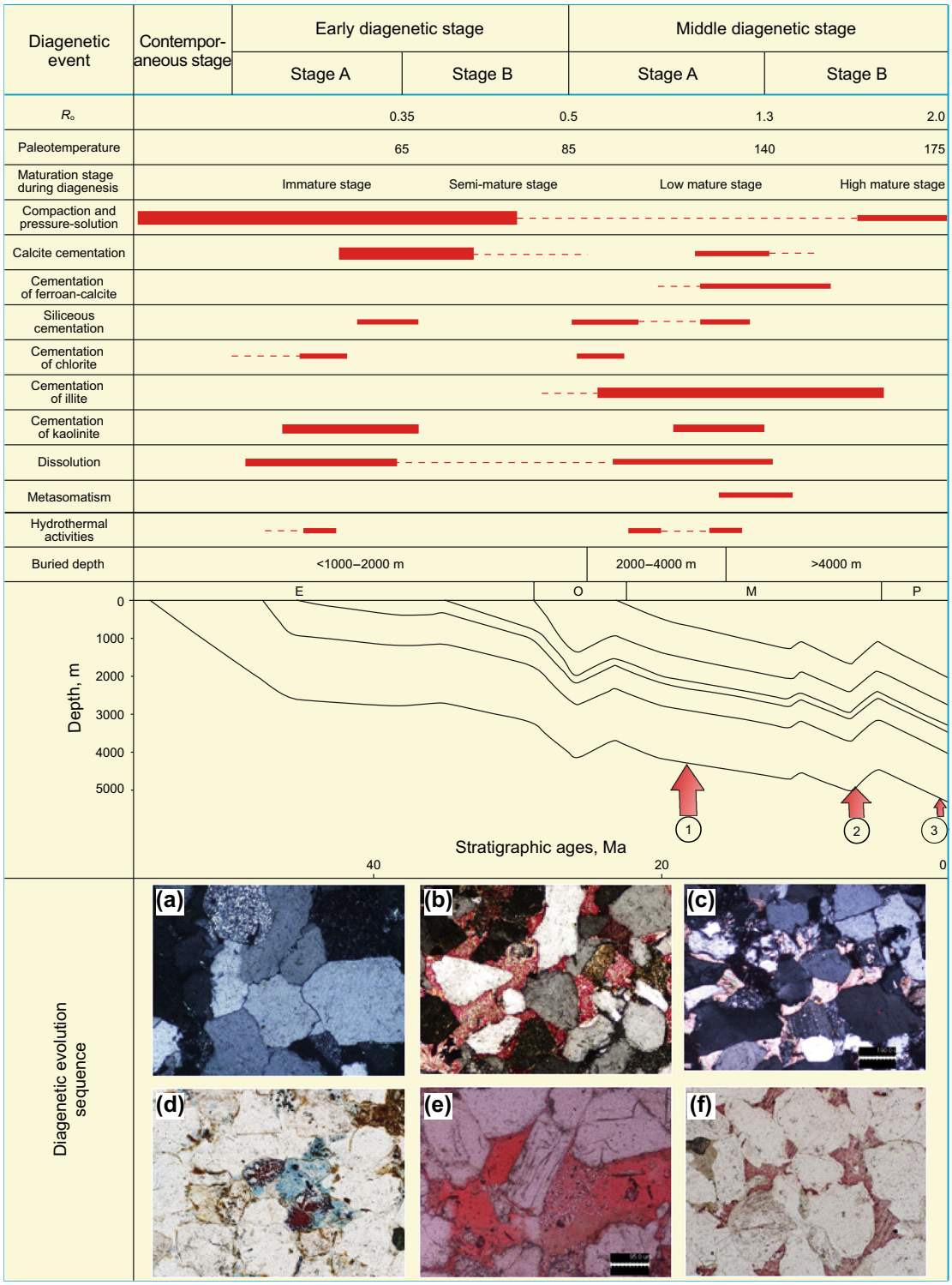

Fig. 3 The coupling diagram of diagenetic evolution, hydrothermal activity and oil and gas charging in research in the Xihu Depression (1) the first oil and gas charging stage, (2) the second oil and gas charging stage, (3) the third oil and gas charging stage. **a** W10, 3148.6 m, ×100, Mechanical-chemical compaction, **b** W8, 3410 m, ×100, Early calcite cementation, **c** W5, 3725.79 m, ×100, Quartz secondary enlargement—Late calcite cementation—The feldspar was metasomatized by calcite, **d** W5, 3725.32 m, ×100, Ferroan calcite, **e** J1, 3296.12 m, ×20, Feldspar dissolution and kaolinite precipitation, **f** W10, 3444.2 m, ×100, Chlorite rims—Quartz secondary enlargement—Late calcite cementation

scattered electronic image is 2.5 nm. The experimental temperature is 21 ± 4 °C; the humidity is ≤ 65% RH.

(4) A Rigaku D/Max-2500PC fully automatic powder X-ray diffractometer was utilized to measure the compositions (total rock + clay) and mineral contents of sample powders. The samples were ground to less than 40 μm, and then pressed to make specimens for testing. The diffraction peak intensity of different mineral components is generally expressed by the integral strength following subtraction of the background. The working voltage of the diffractometer was 40 kV, the electric current is 40 mA, and the angular accuracy of the equipment is better than 0.02 degrees. THMS600G automatic hot and cold stations (Linkam company) and A Nikon E600 microscope was used to measure temperature of fluid inclusions, the determination of temperature ranges from − 196 °C to 600 °C, and the temperature precision is ± 0.01 °C.

(5) A J&M microspectrophotometer (Germany) and a Zeiss polarizing microscope (Germany) were used to measure the vitrinite reflectance, R_o, of the samples. During the study, the characteristics of the microcomponents of the organic matter in the samples were examined under 50 times magnification and with a reflectance range of 0.59%–10%.

(6) A Zeiss polarized fluorescence microscope A1-HBO 100 (Germany) and a Cooling–Heating Stage Linkam—TH600 were used to analyze the homogenization temperatures of the inclusions in rock samples. After observing the microscopic characteristics of the fluid inclusions under the polarizing fluorescence microscope, the inclusions were placed in the Cooling–Heating Stage apparatus. The temperature at which the gas phase or liquid phase of the fluid inclusions disappears is the homogenization temperature. The temperature of the experimental environment is 20–25 °C, the humidity is 30%, and the temperature precision is ± 1 °C.

(7) An Autopore 9500 made by the Mike Murray Feldman Instrument Co. Ltd. (Shanghai) was used to measure pore-throat radius. The maximum external pressure applicable was 60,000 psia.

4 Results

4.1 Petrological evidence for the influence of magmatic hydrothermal fluids

Analysis of 74 thin sections and SEM analyses of 22 samples from the 14 wells from the southern Xihu Depression showed that the quartz content of the deep sandstone reservoirs in the Xihu Depression ranges between 60% and 95% with an average value of 77%. The feldspar content ranges between 10% and 27% with an average value of 11.1%. The feldspars are primarily potassium feldspars with some acidic plagioclase. The lithic grain content varies between 5% and 40% with an average of 11.6%. Lithic grains consist mainly of argillaceous, calcareous, and siliceous sedimentary lithic grains or low-grade metamorphic lithic grains with minor amounts of volcanic and intrusive lithic grains. Three main petrological characteristics were identified related to high pressures and hydrothermal fluids associated with magma intrusion. These were: brittle fractures and alteration of skeleton particles, precipitation of associated hydrothermal minerals, and the thermal alteration of the country rocks.

Brittle fracturing and the alteration of skeleton particles were observed in the clastic rocks near the magmatic body in all 10 wells. For example, well-log analysis in wells W1, W6, W7 and W9 led to the identification of magmatic bodies in the Yuquan Formation (N_1^2y), Longjing Formation (N_1^1l), Huagang Formation (E_3h), Pinghu Formation (E_2p), and Baoshi Formation (E_2b). Brittle fractures in clastic particles located near magmatic bodies were seen in thin section (Fig. 4).

Celestite ($SrSO_4$), apatite ($Ca_{10}(PO_4)_6(OH)_2$), barite ($BaSO_4$), and cerous phosphate ($CePO_4{\cdot}H_2O$) were identified from environmental scanning electron microscope observations and energy spectrum analysis of samples in wells W6, W7, and W9 (Fig. 5).

The examination of thin sections and scanning electron microscope analyses showed that large amounts of minerals in the reservoirs were related to hydrothermal activity, including the formation of authigenic quartz and transformation of clay minerals.

Authigenic quartz cement was well developed in the study area and was mostly in the form of secondary overgrowths and microcrystalline quartz (Fig. 6a, d). Intraparticle fractures in the quartz grains were found in Well W7 at 3718.32 m using cathodoluminescence (CL). During CL examination, quartz generally shows a brown, bluish-purple, and/or non-luminescent character (Fig. 6b). The quartz at a depth of 3719.12 m was bluish-purple, or light brown and non-luminescent; the secondary quartz at a depth of 2258.58 m was bluish-purple under CL (Fig. 6c). The characteristics of quartz under CL are known to be closely related to diagenesis temperature, with the color changes gradually from blue to bluish-purple as the temperature increases.

Sixty-seven sandstone samples from 1113 to 4500 m in Well W7 were used to identify the different clay minerals contents using X-ray diffraction. The results showed that the content of kaolinite decreased with increasing depth, while illite content generally increased with increasing depth. Illite was identified in Well W7 at a depth of approximately 1000 m and accounted for 40%–60% of the total

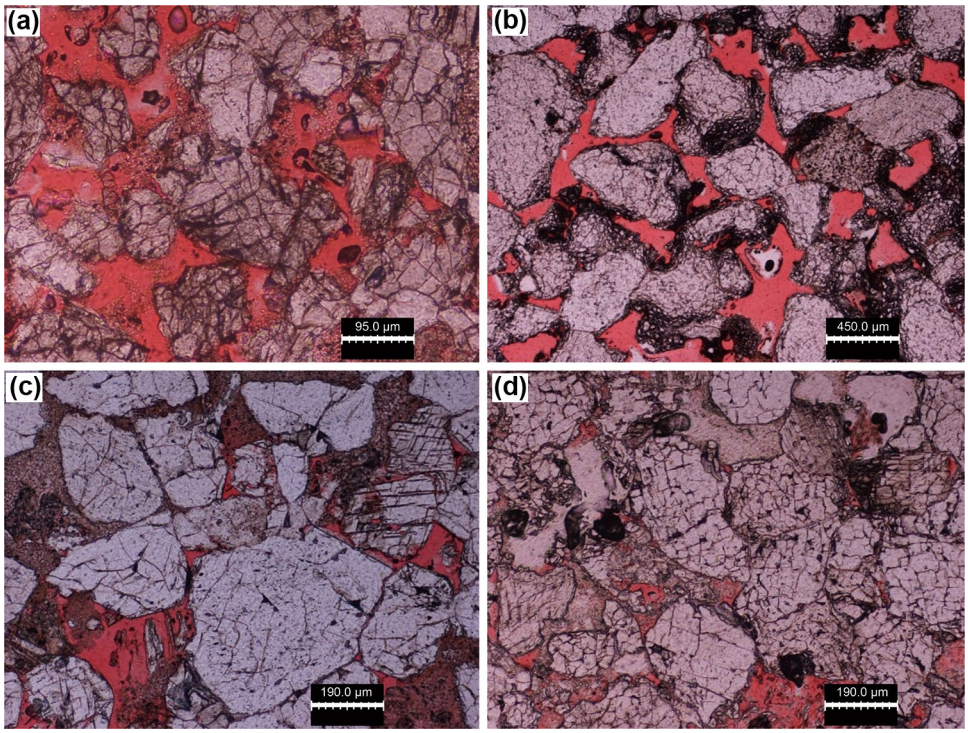

Fig. 4 Brittle fractures inside quartz grains. **a** W1, 2215.58 m, **b** W7, 3443.97 m, **c** W6, 4052.62 m, **d** W9, 4198.34 m

clay minerals (Fig. 6). Based on SEM observations, illite occurs in several locations, including pore wall linings, solid inclusions in clastic grains, and pore-filling authigenic illite. The pore lining authigenic illite crystal morphology is fine needles perpendicular to the surfaces of the clastic particles (Fig. 6e–h). Where illite occurs as solid inclusions in clastic grains, the crystals form parallel to the surface of the grains and were not present in contacts between particles. The pore-filling illite was found at the exterior margins of the pore wall lining. Illite is an authigenic clay mineral that is known to occur within a temperature range of 120–300 °C (Yu et al. 2012).

Under the normal geothermal gradient, 3.4–3.5 °C/100 m and considering the burial history of the Xihu Depression, significant amounts of illite should begin to appear at depths exceeding 3200 m. At this depth, formation temperature is approximately 120 °C. Kaolinite becomes unstable at temperatures between 120 and 150 °C and transforms into illite under potassium-rich conditions (Huang et al. 2009) (Eq. (1)), resulting in increased illite content. Substantial amounts of illite were identified at shallow depths (approximately 1000 m) in well W7. Therefore, there is a negative correlation between kaolinite and illite at temperatures between 120 and 150 °C in well W7 (Fig. 6).

$$3Al_2Si_2O_5(OH)_4(\text{kaolinite}) + 2K^+ \rightarrow 2KAl_3Si_3O_{10}(OH)_2(\text{illite}) + 2H^+ + 2H_2O \quad (1)$$

4.2 Fluid inclusion temperature indicators

Fluid inclusions are relatively well developed in the healed fractures in quartz samples from the study area. For example, gas–liquid, two-phase aqueous fluid inclusions were identified along healed fractures in the quartz grains in well W9 located in the Tianwaitian main fault (Fig. 7a). At a depth of 2824.6 m, the homogenization temperatures of the inclusions range from 131.5 to 139.1 °C with an average value of 134.2 °C, which is much higher than the regional burial temperature of 118 °C at this depth (geothermal gradient of 3.7–3.8 °C/100 m in the southern of Central anticline). Similarly, the highest measured homogenization temperature was 156.6 °C at a depth of 3294.8 m (Fig. 7b), which was much higher than the regional burial temperature of 131.1 °C at this depth, assuming a normal geothermal gradient.

Thirty-five samples from six wells in the Sudi tectonic belt, taken between 3294.8 and 3365.8 m, were analyzed for fluid inclusions. The results showed that the homogenization temperatures of the fluid inclusions were in the ranges of 130–140 °C and 150–160 °C at depths of 2748.5–3423.7 m (Fig. 8a). Twenty-five samples from two wells in the Xiling tectonic belt taken between 3248.5 and 3423.7 m were analyzed for fluid inclusions, and the homogenization temperatures of the fluid inclusions varied from 120 to 130 °C and 150 to 160 °C with sample depths between 3294.8 and 3365.8 m (Fig. 8b). With reference to

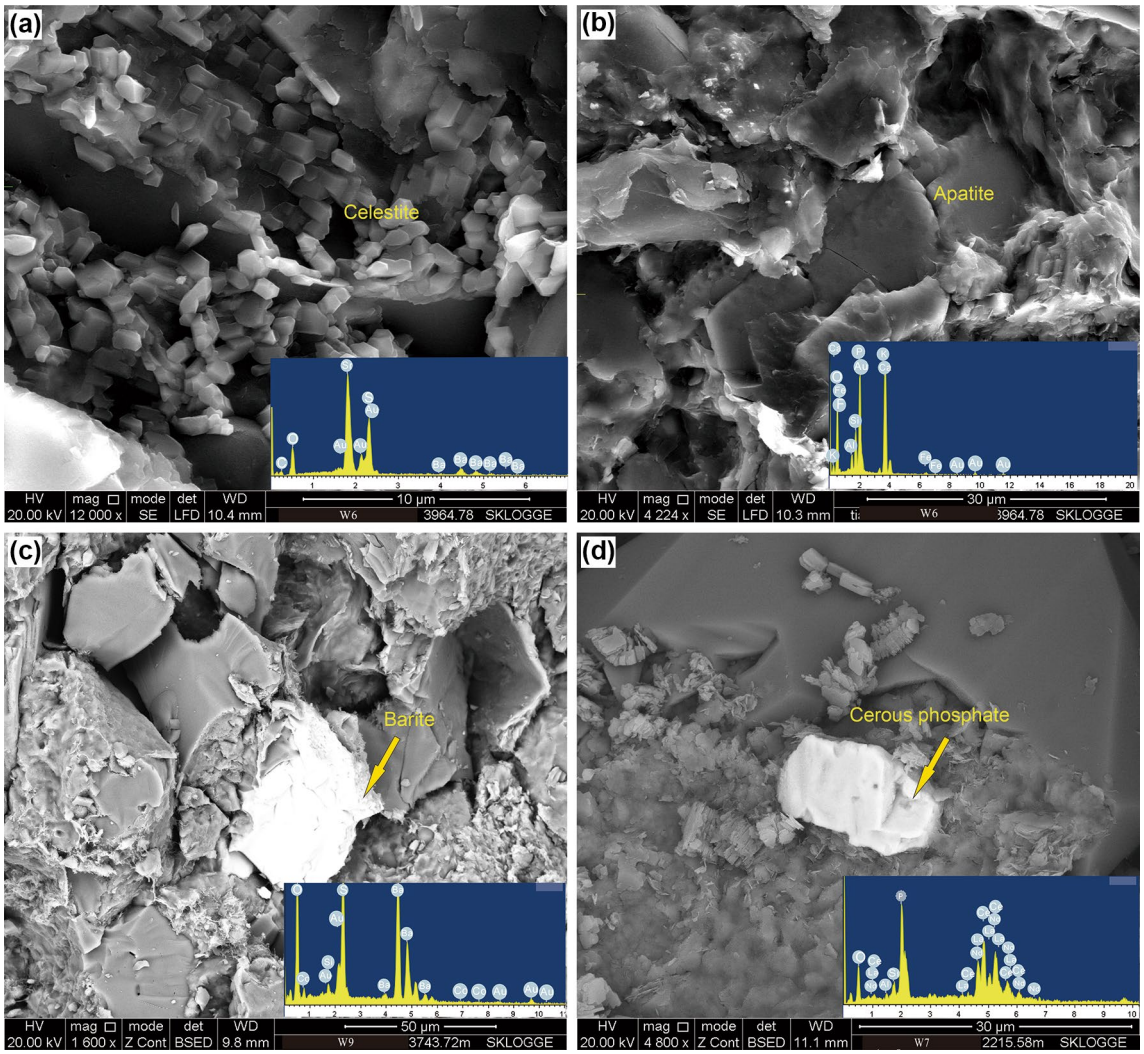

Fig. 5 Hydrothermal minerals identified by FEG-SEM backscatter electron imaging and EDS in the Xihu Depression. **a** Celestite ($SrSO_4$), W6, 3964.78 m; **b** Apatite ($Ca_{10}(PO_4)_6(OH)_2$), W6, 3964.78 m; **c** Barite ($BaSO_4$), W9, 3743.72 m; **d** Cerous phosphate ($CePO_4{\cdot}H_2O$), W7, 2215.58 m

the Paleogene geothermal gradient of 3.4–3.8 °C/100 m for this region (Zhou 2003), and considering the burial history, the normal burial temperature at the sampled depths should only be 108–126 °C in the Sudi Structural Zone and 120–127 °C in the Xiling Tectonic Zone. The abnormally high fluid inclusion paleotemperatures were observed in the study area.

4.3 Fault control on vitrinite reflectance and intrusive related hydrothermal fluids

Vitrinite reflectance (R_o) is an effective index to determine organic matter maturity and is related to kerogen type, temperature, and pressure (Yu et al. 2012). In general, R_o increases gradually with burial depth at a relatively constant rate (Su et al. 2016; Liu et al. 2017).

R_o values at various depths from three wells (W1, W7, W9) close to fault zones and affected by magmatic bodies and hydrothermal fluids were measured using a J & M microspectrophotometer. R_o values showed thermal anomalies at the following depth ranges. In well W1, the highest R_o value (0.79%) was obtained at depths between 3060 and 3200 m (Fig. 9a). In well W7, the highest R_o values were identified at 2408–2574 m (the range of R_o is 0.58%–0.65%), 3292–3354 m (the range of R_o is 1.22%–1.39%), and 4084–4175 m (the range of R_o is 0.92%–1.39%) (Fig. 9b). In well W9, the R_o values were 1.07%–1.12% at depths of 3427–3600 m (Fig. 9c). At these intervals, the measured R_o values were higher than the expected values (the range of R_o is 0.89%–0.96%) at corresponding depths in normal conditions. Moreover, magmatic rocks were identified based on well-log data at similar depths to where the high R_o values were obtained.

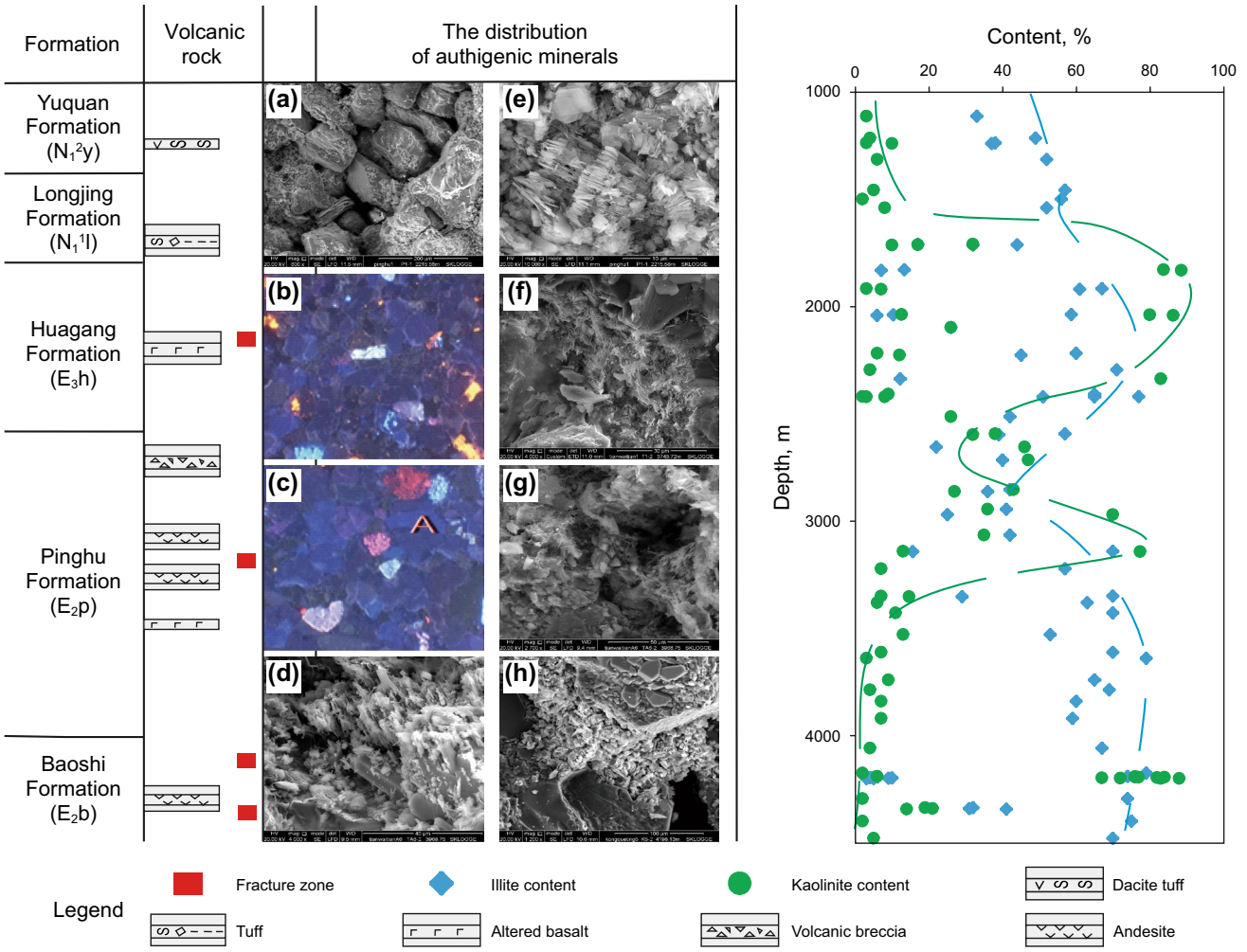

Fig. 6 The petrological characteristics of minerals affected by hydrothermal alteration in well W7, Xihu Depression. Secondary quartz development (**a** 2215.58 m); the CL characteristics of quartz (**b** 3718.32 m, **c** 3719.12 m); authigenic quartz (**d** 3968.75 m); kaolinite converted into illite (**e** 2215.58 m, **h** 4198.13 m); the silk-thread variant of illite (**f** 3743.72 m, **g** 3968.75 m)

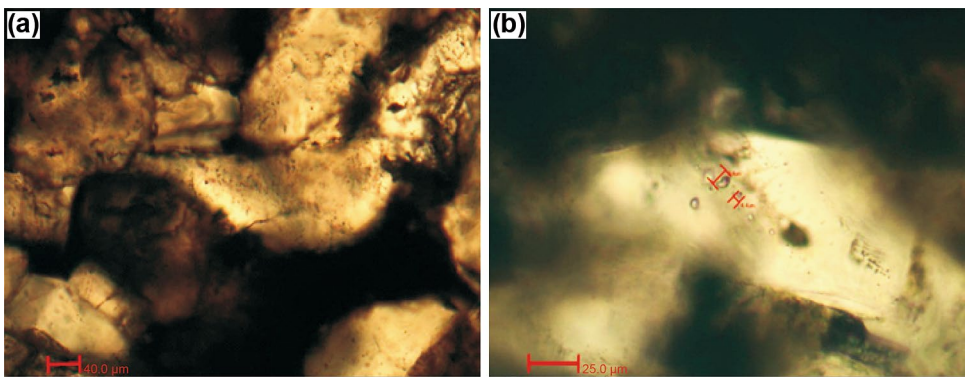

Fig. 7 Micrographs of fluid inclusions from the Xihu Depression **a** W9, 2824.6 m, 20×, gas liquid hydrocarbon inclusions distributed along quartz healing cracks; **b** W9, 3294.8 m, 50×, brine inclusions distributed along quartz healing cracks

The comparison of 117 R_o values between different wells shows a strong relationship with the observed distribution of structural features. The samples from W1, W6, W7, W8, W9 were located closely to fault zones and affected by magmatic intrusion and hydrothermal fluids. These showed consistently higher R_o values than samples from Q2, J1 that were not affected by magmatic intrusions (Fig. 10). Spikes in R_o values were identified at depths of 2400–2500 m, 3400–3500 m, and 4000–4300 m. For example, 0.65% at 2408 m, 1.22% at 3292 m, and 1.39% at 4175 m are

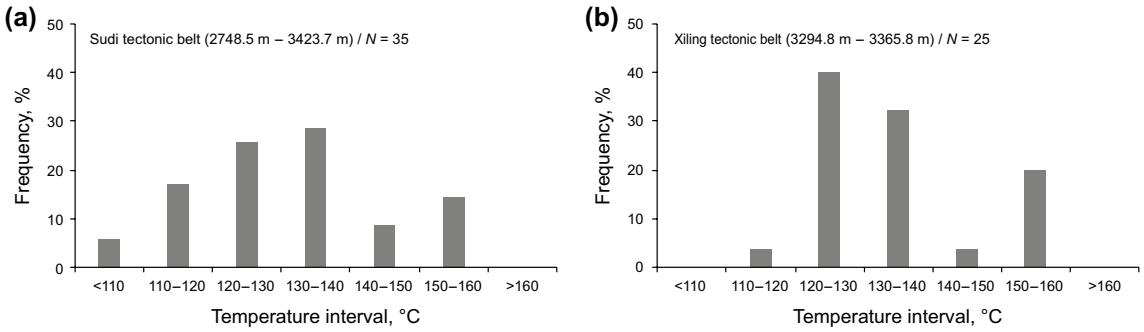

Fig. 8 Graphical representation of the statistical distribution of fluid inclusions and temperature in the Xiling and Sudi tectonic belts, Xihu Depression

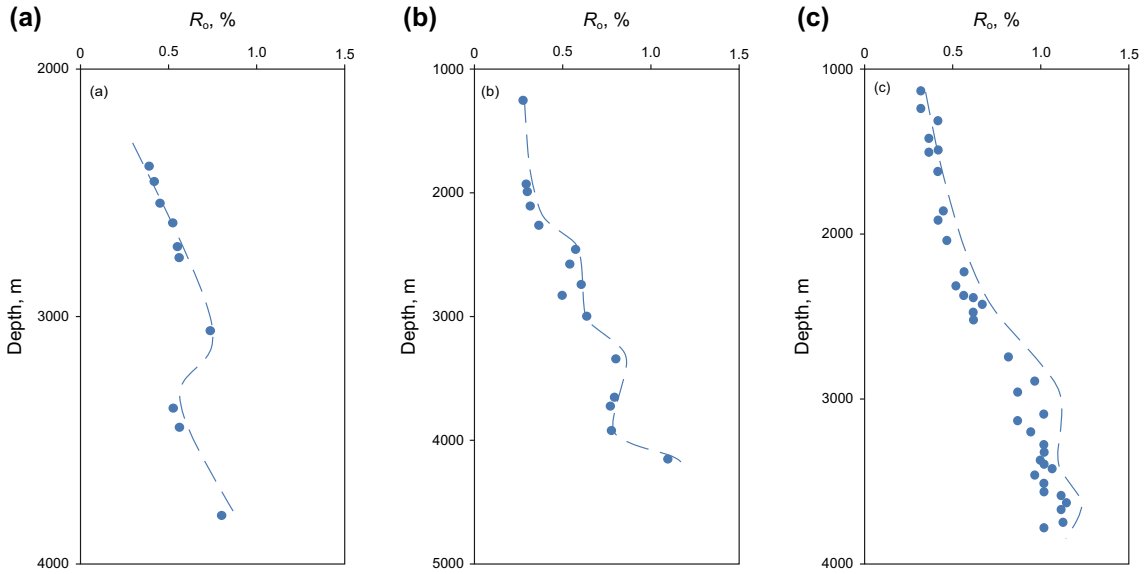

Fig. 9 The relationship curve between R_o values and depths. **a** well W1, **b** well W7, **c** well W9

considerably higher than the R_o values at neighboring depths ranges. In contrast, R_o values from 109 samples that were not affected by fault activity increased approximately linearly from 0.3% to 1.0% as depth increased.

The CO_2 content of the natural gas sampled from wells located near fault zones (such as W1, W3, W7, W7, W8, and W9) is relatively high, exceeding 7.35% (W7), (the highest value is 12.7% (W9). By contrast, the CO_2 content in wells far from fault zones was 0.58%–2.37%. This can be interpreted as being the result of vertical migration of deep gas along the fault systems (Fig. 11a). The SO_4^{2-} content of the formation water in wells W1, W3, and W8 that intersected fault zones, exceeded 2000 mg/L, whereas SO_4^{2-} content in wells far from fault zones was less than 1000 mg/L (Fig. 11b). The higher amounts of SO_2 near the fault zones were the result of upward migration of deep hydrothermal fluids, which reacted with pore water and generated large amounts of sulfate anions. These results demonstrate the effect of fractures on hydrothermal fluid migration.

4.4 The reservoir porosity characteristics

As depth increases, the porosity and permeability of the 403 samples from the five wells (G1, G2, J1, J2, Q2), which were not affected by the hydrothermal alteration and lie distal to any faults decreases. The 442 samples from wells W1, W4, W5, W7, which were affected by hydrothermal activity, showed abnormally high porosity at intervals of approximately 2400–2500 m, 3400–3500 m, and 4000–4300 m depth (Fig. 12), with average values reaching 23.1%, 19.6%, and 17.5%, respectively. As an example, the porosity at 3441 m in well W1 was as high as 20% and showed pores with an average

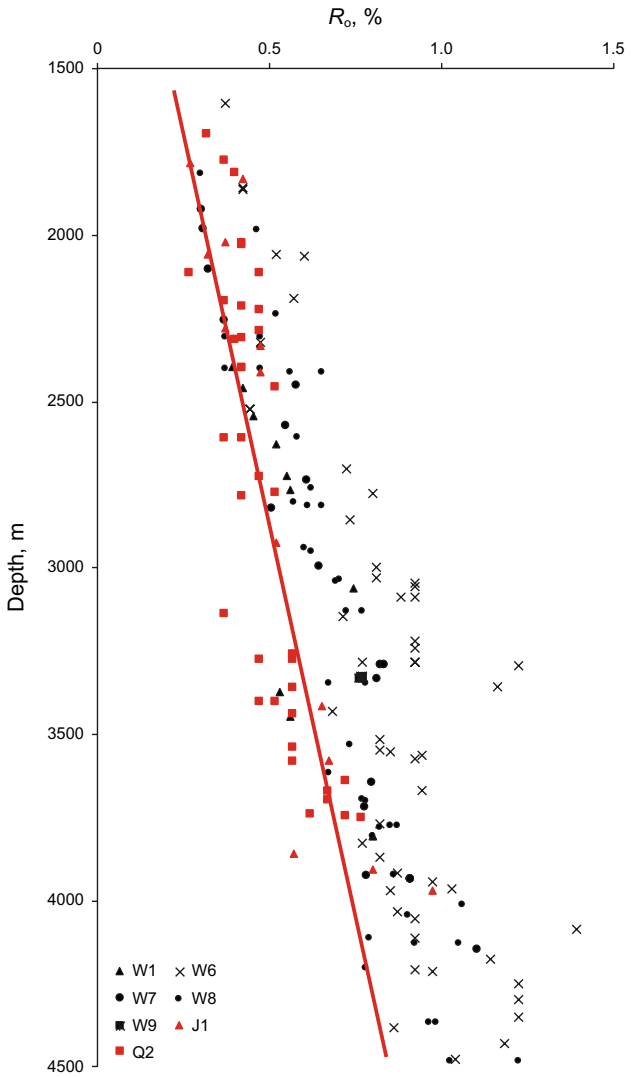

Fig. 10 The relationship curve between R_o values and depth from different wells

pore-throat radius of 13.2 μm. The maximum porosity of well W6 between 3964 and 4175 m was as high as 14.6% with an average pore-throat radius of 4.12 μm (these data were provided by Sinopec Shanghai Oil and Gas Branch). The mercury injection capillary pressure (MICP) analysis revealed that the pore-throat radius ranged from 1 to 40 μm. The pore-throat assemblages were mainly medium pores with medium throats, small numbers of large pores with large throats and small pores with thin throats (Fig. 12). Based on thin section examination, the main types of pores present have been categorized and include combinations of interparticle dissolution pores, interparticle pores, intraparticle dissolution pores, interparticle micropores, moldic pores and dissolution vugs. Well W1 located in the Baoshi Fault Zone and affected by hydrothermal fluids, encountered tuffaceous rocks at 3200 m. At this depth, quartz particles in the reservoirs were subjected to brittle fracturing and alteration, and vitrinite reflectance was abnormally high. Andesite, diorite, tuffaceous rocks, and altered dacitic rock were found at approximately 4800 m in well W6 which was located in the Chunxiao Fault Zone. The vitrinite reflectance in mudstones at this depth reached 1.35%. At a depth of 3840–4275 m, well W7 located in the Tianwaitian Fault Zone and affected by hydrothermal fluids, encountered tuff breccia, tuff, granite, granodiorite rocks. At these depths, the maximum porosity was 25.9% and the minimum was 1.5%, and the average value was 14.5% (Table 2). 44% of the sand thickness (29.5 m) of the Pinghu Formation was seen to have porosities greater than 14% (3516–4645 m) (Fig. 12).

For the wells close to fault zones affected by hydrothermal activity, thin section and SEM observations revealed that the dissolution of potassium feldspar, volcanic detritus, metamorphic lithics and phyllites by CO_2-rich acidic fluids was extensive, resulting in the formation of intergranular dissolved pores and moldic pores. Based on the comparison of porosity and pore-throat characteristic of the samples from these wells, large differences in dissolution distribution are believed to arise from the influx of magmatic hydrothermal fluids in fracture zones. A multi-well correlation exercise was carried out using the porosity logs and seismic and volcanic detritus interpretation results. It is noted that

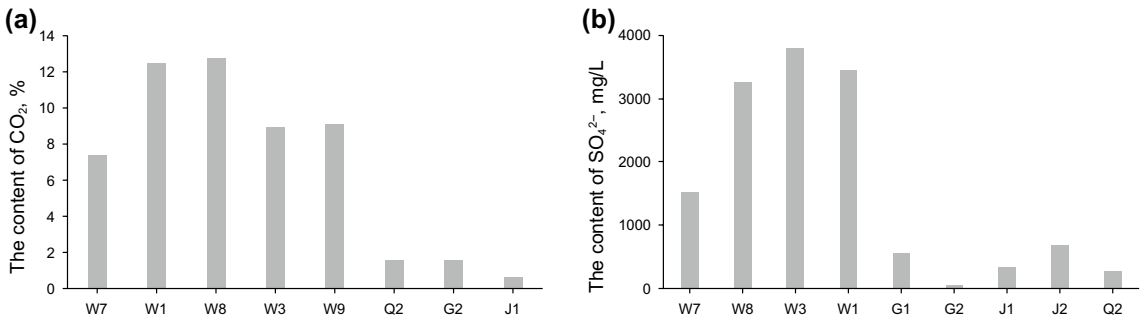

Fig. 11 The measured CO_2 content in gas component analysis (**a**) and the content of SO_4^{2-} in formation water, Xihu Depression (**b**)

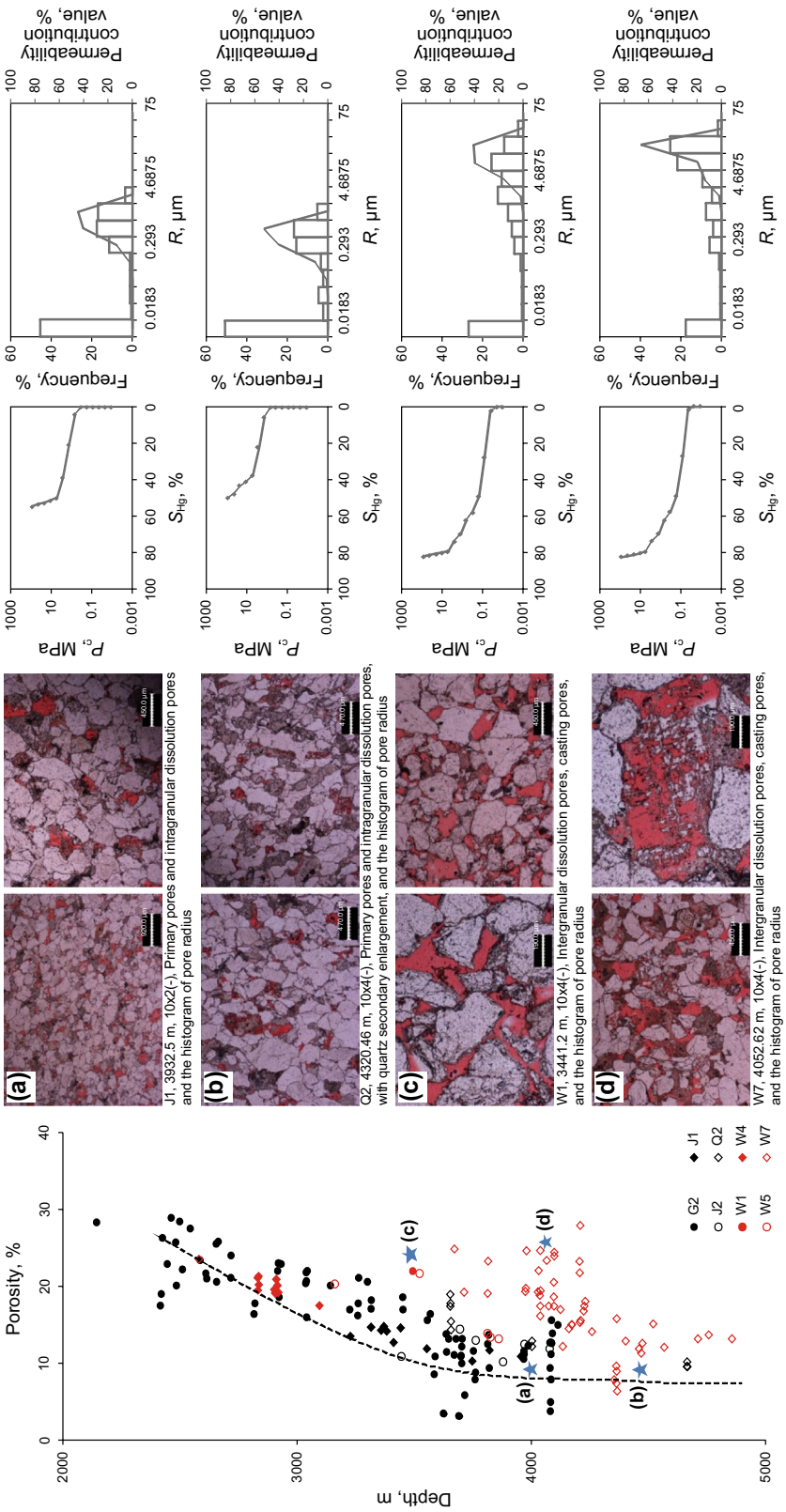

Fig. 12 The relationship curves for porosity and depth, pore types and the histogram of pores radius in wells affected by hydrothermal fluids (particle data from the Shanghai Branch of CNOOC, China)

Table 2 The porosity values of wells

District	Well	Depth, m	Porosity, %		
			Φ_{max}	Φ_{min}	Φ_{avg}
Fault zone	W1	3440–3447	18.9	15.1	17.0
	W4	2810–2897	18.8	16.6	17.4
	W5	3792–3840	17.8	10.7	12.7
	W7	3775–4200	25.6	1.5	14.5
Far from fault	G2	2000–3000	32.8	13.9	20.8
		3000–4000	19.5	0.7	10.7
		4000–4072	13.1	1.2	8.7
	J1	3724–3984	11.1	3	8.3
	J2	3420.2–4531	14.6	3.1	10.4
	Q2	3633–4646	16.5	7.1	12.2

The sample location is marked on the well profile in Fig. 12

the distribution of the volcanic detritus is associated with the existence of faults. For example, the net thickness of high porosity sands (over 14% porosity) is much higher in Wells W1, W3, W6 and W7, sited in the Baoshi, Chunxiao and Pinghu fault complexes than those from Wells G2, Q2 and J2 where no faults or volcanic detritus are present. According to the porosity logs, higher porosity is observed adjacent to the faults, with porosity values falling in areas away from the faults (Fig. 13, Table 2).

5 Discussion

Previous studies of the burial and thermal history of the Xihu Depression suggested that the thermal effects of magmatic intrusives were detectable in the southern part of the central uplift zone and the Sudi Structural Zone (Zhou 2003; Su et al. 2016).

The impact of intruded magma and hydrothermal fluids on the surrounding rocks has been shown significantly in this paper. The following phenomena are described in the study: brittle fracturing and clastic particle alteration. When magma intruded into consolidated country rock, the pressure from this sudden influx resulted in brittle fracturing of the country rocks, clastic particles expanded, cracked and subsequently healed during the upwelling of deep hydrothermal fluids (Fig. 4). Other observed effects including: the precipitation of unique hydrothermal minerals (Fig. 5) and illite alteration, and kaolinite becomes unstable at temperatures between 120 and 150 °C and transforms into illite under potassium-rich conditions (Huang et al. 2009), resulting in increased illite content. The influence of hydrothermal fluids and the local baking effects of magmatic rocks on the surrounding rock strata (Fig. 6) results in the presence of abnormally high temperatures in fluid inclusions (Fig. 7) and anomalous vitrinite reflectance (Fig. 9). These phenomena in the study area are interpreted as being related to the two magmatic thermal events that occurred at the end of the Early Miocene and the Late Miocene (Yang et al. 2001). The deep faults that propagate from the basement act as a regional conduit system for upward migration of hydrothermal fluids to the reservoirs, and this results in significant modification and alteration. The high-temperature magma consisting of a volatile silicate melt released significant amounts of heat and volatiles when migrating upwards and cooling (Tao and Xu 1994). This process resulted in abnormally high geothermal gradients and affected the prospectivity of the surrounding rocks, especially the migration of alkanes and

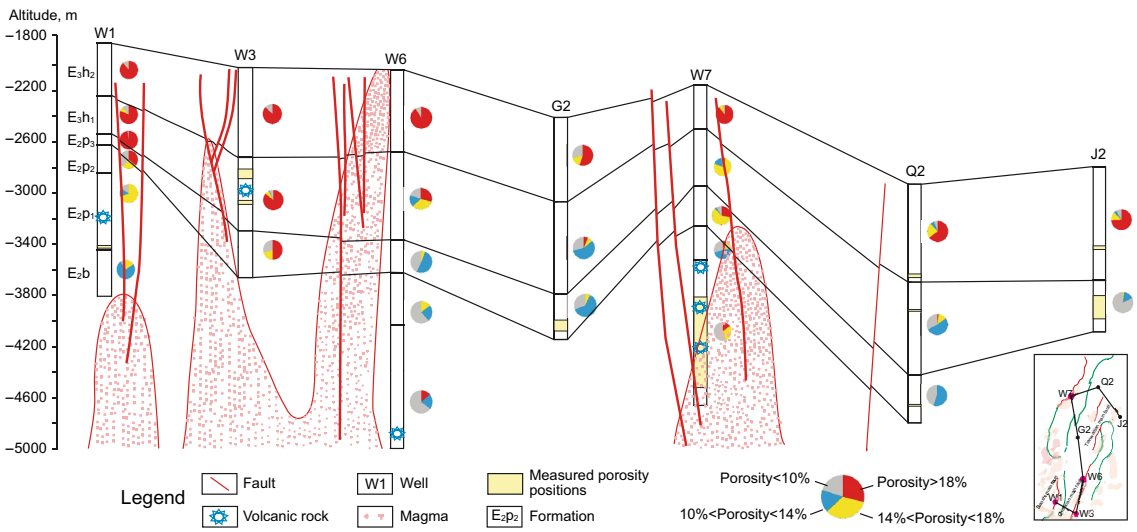

Fig. 13 The difference in pore characteristics in samples from wells affected by hydrothermal fluids near faults and from samples not affected by hydrothermal fluids, far from faults (Pie Chart: Ratio of sand body thickness in different porosity intervals to total sand thickness)

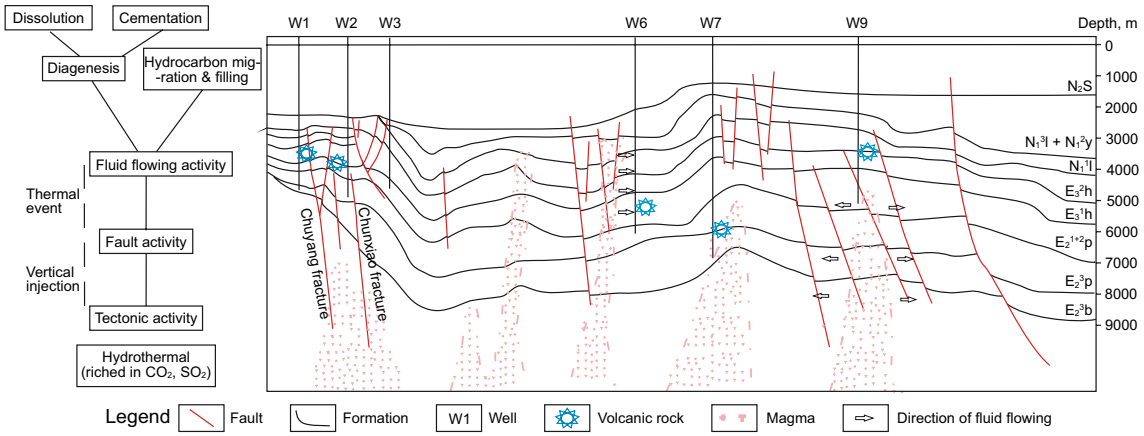

Fig. 14 The dissolution model of hydrothermal fluids in the Xihu Depression

reservoir diagenesis of the formations underlying or overlying the intrusives.

Based on the results above, the depths where abnormally high porosity zones were encountered were consistent with the depths where the magmatic intrusions and thermal fluid activity were noted.

The mechanism of dissolution of alkaline minerals by late CO_2-rich acidic fluids is closely linked to the influence of magmatic hydrothermal fluids on the thermal evolution of source rocks discussed in this paper. The hydrothermal fluids related to the intrusives could carry organic acids and/or fluids rich in CO_2 and SO_2, decreasing the pH of the host rock diagenetic environment (Eqs. (2)–(4)) resulting in dissolution of feldspar grains and carbonate cements (the dissolution reaction is shown in Eqs. (5)–(10)) (Wang et al. 2017a, b), leading to secondary dissolution porosity in the host rocks. As illustrated in Eqs. (6)–(8), the dissolution of feldspar leads to the precipitation of quartz as overgrowth cements.

$$\mathrm{RCOOH} = \mathrm{RCOO^-} + \mathrm{H^+} \tag{2}$$

$$2\mathrm{CO_2} + 2\mathrm{H_2O} = 2\mathrm{H_2CO_3} = 3\mathrm{H^+} + \mathrm{CO_3^{2-}} + \mathrm{HCO_3^-} \tag{3}$$

$$\mathrm{SO_2} + \mathrm{H_2O} = \mathrm{H_2SO_3} \quad \mathrm{H_2SO_3} + \mathrm{O_2} = 2\mathrm{H^+} + \mathrm{SO_4^{2-}} \tag{4}$$

$$\begin{aligned} &\mathrm{CaCO_3} + \mathrm{H^+} = \mathrm{Ca^{2+}} + \mathrm{HCO_3} \\ &\mathrm{Ca \cdot Mg(CO_3)_2} + 2\mathrm{H^+} = \mathrm{Ca^{2+}} + \mathrm{Mg^{2+}} + 2\mathrm{HCO_3^-} \end{aligned} \tag{5}$$

$$\begin{aligned} &2\mathrm{KAlSi_3O_8}(\text{potash feldspar}) + 2\mathrm{H^+} + \mathrm{H_2O} \\ &= \mathrm{Al_2Si_2O_5(OH)_4}(\text{kaolinite}) + 4\mathrm{SiO_2} + 2\mathrm{K^+} \end{aligned} \tag{6}$$

$$\begin{aligned} &2\mathrm{NaAlSi_3O_8}(\text{soda feldspar}) + 2\mathrm{H^+} + \mathrm{H_2O} \\ &= \mathrm{Al_2Si_2O_5(OH)_4}(\text{kaolinite}) + 4\mathrm{SiO_2} + 2\mathrm{Na^+} \end{aligned} \tag{7}$$

$$\begin{aligned} &2\mathrm{CaAlSi_3O_8}(\text{calcium feldspar}) + 2\mathrm{H^+} + \mathrm{H_2O} \\ &= \mathrm{Al_2Si_2O_5(OH)_4}(\text{kaolinite}) + 4\mathrm{SiO_2} + 2\mathrm{Ca^+} \end{aligned} \tag{8}$$

$$2\mathrm{Ca^{2+}} + \mathrm{C^mO_3^-} + \mathrm{C^0O_3^-} = 2\mathrm{CaCO_3} \tag{9}$$

$$2\mathrm{Ca^{2+}} + \mathrm{C^mO_3^-} + 2\mathrm{RCOO^-} = \mathrm{CaC^mO_3} + \mathrm{Ca(RCOOH)_2} \tag{10}$$

The incursion of high-temperature hydrothermal fluids from the crystalline basement is thought to have increased formation temperatures in the study area, as average geothermal gradients in the region are as high as 4.22 °C/100 m as interpreted from anomalously high vitrinite reflectance values in the surrounding rocks. These hydrothermal incursions would accelerate the thermal maturation of organic matter, releasing large amounts of short-chain organic acids. These relatively low molecular weight organic acids can form organic acid anions with aluminum complexes, enhancing the dissolving capacity of Al and Si in aqueous solution, and increasing some of rock element migration ability in groundwater. Thus, the transformation of the silicate mineral characteristics and connecting throat pore surface properties cause the variation of oil reservoir porosity and permeability of rock mass (Oelkers and Schott 1995; Guo et al. 2003; Zhang et al. 2009).

The high temperatures also enhance the dissolution of feldspar in the acidic conditions and produce secondary porosity (Zhao 2005). Based on these observations, the research team developed a preliminary model to account for reservoir development in the region considering the action of hydrothermal fluids associated with igneous intrusives in the Xihu Depression (Fig. 14). The pores generated during the dissolution process improved reservoir quality, but dissolution products, such as Ca^{2+} and Mg^{2+}, could be carried by the hydrothermal fluids to overlying strata above or to the peripheral regions where they could be precipitated as

carbonate cements, reducing the reservoir quality in those areas. Subsequent research should concentrate on how this precipitation of mobile ions affects pore development and porosity in peripheral areas.

6 Conclusions

The following conclusions can be drawn from the present study:

(1) Three Cenozoic episodes of volcanic activity accompanied by magmatic intrusions that caused brittle fracturing of the surrounding sandstones have been identified. Quartz and feldspar particles show cracking on their margins related to thermal expansion due to heating. Because of the high temperatures, and the CO_2 and SO_2 which were carried by the hydrothermal fluids associated with the magmatic intrusions, the host sandstones were subjected to thermal alteration, which led to the precipitation of an assemblage of hydrothermal minerals such as celestite, zircon, apatite, barite, and cerous phosphate. In addition, authigenic quartz and illite were formed due to the influence of hydrothermal fluids on the surrounding rocks.

(2) The fluid inclusion density in the southern part of the central anticlinal zone was abnormally high due to the influence of hydrothermal fluids. R_o values indicated three depth intervals of anomalous high temperatures: 2400–2500 m, 3400–3500 m, and 4000–4300 m, these being spatially and temporally coincident with episodes of intrusion. The magmatic body and hydrothermal fluids led to accelerated maturation of organic matter in the source rocks. As the hydrothermal fluids migrated upward along fault zones, local geothermal gradients were increased as indicated by higher R_o values in the areas close to the faults and intrusive bodies.

(3) The distribution of hydrothermal fluids was found to be consistent with the orientation of the fault systems. The secondary dissolution caused by the hydrothermal fluids related to the intrusives was most abundant in areas deeper than 3500 m and close to fault zones. The hydrothermal fluids carried dissolved CO_2 and SO_2, and migrated along unconformities, faults and fractures, and accelerated the thermal maturation of organic matter in the source rocks, this resulted in further release of organic acids and CO_2. The pH of the diagenetic fluids decreased, and this led to dissolution of the feldspar, volcanic lithic grains, and early carbonate cements. These reservoirs are dominated by secondary porosity, which includes interparticle dissolution pores, intraparticle dissolution pores and moldic pores.

Furthermore, the hydrothermal fluids associated with intrusives had two main impacts on reservoir properties: (a) formation of secondary dissolution pores improving the reservoir quality and (b) precipitation of authigenic minerals from the dissolution products, such as Al^{3+}, Ca^{2+} and Mg^{2+}, precipitated as cement in the overlying strata or the peripheral regions when temperature, pressure or pH conditions changed. Finally, the porosity in the reservoirs decreased and the anisotropy increased. So, upcoming research will focus on the quantitative characterization of the dissolution and cementation of the deep hydrothermal fluids on the clastic reservoirs and establish a corresponding model.

Acknowledgements This work was funded by the National Natural Science Foundation of China (Grant No. 41502135). The authors are grateful to the State Key Laboratory of Oil and Gas Reservoir Geology and Exploitation and the anonymous reviewers for their extraordinary advice.

Open Access This article is distributed under the terms of the Creative Commons Attribution 4.0 International License (http://creativecommons.org/licenses/by/4.0/), which permits unrestricted use, distribution, and reproduction in any medium, provided you give appropriate credit to the original author(s) and the source, provide a link to the Creative Commons license, and indicate if changes were made.

References

Agusto M, Tassi F, Caselli AT, et al. Gas geochemistry of the magmatic-hydrothermal fluid reservoir in the Copahue-Caviahue Volcanic Complex (Argentina). J Volcanol Geotherm Res. 2013;257(2):44–56. https://doi.org/10.1016/j.jvolgeores.2013.03.003.

Cai H, Zhang JP, Tang XJ. Characteristics of the fault systems and their control on hydrocarbon accumulation in the Xihu Sag. Nat Gas Ind. 2014;34(10):18–26. https://doi.org/10.3787/j.issn.1000-0976.2014.10.003 **(in Chinese)**.

Cao B. Study of burial and thermal history of the Huagang Formation tight sandstone reservoir in the central reversal structural belt, Xihu Depression, East China Sea. J Chengdu Univ Technol (Sci Technol Ed). 2016;43(4):1671–9727. https://doi.org/10.3969/j.issn **(in Chinese)**.

Cao Q, Zhou W, Liu Y, et al. Characteristics and origin of deep high-porosity zones in the slope of the Xihu Sag. J Cent South Univ (Sci. Technol). 2017;48(3):751–60. https://doi.org/10.11817/j.issn.1672-7207.2017.03 **(in Chinese)**.

Chen YJ, Ni P, Fan HR, et al. Diagnostic fluid inclusions of different types of hydrothermal gold deposits. Acta Pet Sin. 2007;27(9):2085–2108 **(in Chinese)**.

Charlou JL, Donval JP, Konn C, et al. High production and fluxes of H_2 and CH_4 and evidence of abiotic hydrocarbon synthesis by serpentinization in ultramafic-hosted hydrothermal systems on the Mid-Atlantic Ridge. Diversity of hydrothermal systems on slow spreading ocean ridges. Geophys Monogr. 2010;188(3):265–96. https://doi.org/10.1029/2008GM000752.

Girard JP, Nahon D. Diagenesis of the upper Proterozoic siliciclastic sediments of the Taoudeni Basin (west Africa) and relation to diabase emplacement. J Sediment Pet. 1989;59(2):233–48.

Gu HR, Li CJ, Ye JR. Simulation of generation and expulsion history of the Zhedong Central Anticline Zone in the Xihu Trough, East China Sea. Ocean Pet. 2001;109(3):16–21. https://doi.org/10.3969/j.issn.1008-2336.2001.03.004 **(in Chinese)**.

Guo CQ, Shen ZM, Zhang LY, et al. Corrosion and its mechanism of organic acids on main minerals in oil-gas reservoir sand rocks. Geol Geochem. 2003;31(3):53–7. https://doi.org/10.3969/j.issn.1672-9250.2003.03.010 **(in Chinese)**.

Guo ZQ. On volcanic activity and generation of hydrocarbons. Xingjiang Pet Geol. 2002;23(1):5–10. https://doi.org/10.1016/j.jngse.2016.12.022 **(in Chinese)**.

Hedenquist JW, Henley RW. The importance of CO_2 on freezing point measurements of fluid inclusions: evidence from active geothermal systems and implications for epithermal ore deposition. Econ Geol. 1985;80(5):1379–406. https://doi.org/10.2113/gsecongeo.80.5.1379.

Hu HJ, Tao GB. Tertiary Magmatism and its Relationship with Oil/gas Accumulation in the Xihu Sag, East China Sea. Mar Geol Ser. 1997;3:13–9 **(in Chinese)**.

Huang BJ, Huang HT, Li L, et al. Characteristics of marine source rocks and effect of high temperature and overpressure on organic matter maturation in the Yinggehai–Qiongdongnan Basins. Mar Origin Pet Geol. 2010;15(3):11–8. https://doi.org/10.3969/j.issn.1672-9854.2010.03.002 **(in Chinese)**.

Huang KK, Huang SJ, Tong HP, et al. Thermodynamic calculation of feldspar dissolution and its significance for research into clastic reservoirs. Geol Bull China. 2009;28(4):474–82. https://doi.org/10.3969/j.issn.1671-2552.2009.04.008 **(in Chinese)**.

Liu GD. China sea and adjacent area geology geophysics series map. Beijing: Geological Publishing House; 1992. p. 19–26 **(in Chinese)**.

Liu HM, Zhang S, Song GQ, et al. A discussion of the origin of shale reservoir inter-laminar fractures in the Paleogene Shahejie Formation, Dongying depression. J Earth Sci. 1992;28(6):1064–77. https://doi.org/10.1007/s12583-016-0946-3.

Liu L, Peng XL, Gao YQ, et al. The effect of magmatic activity on clastic rocks and its contribution to diagenesis in northeast and North China Petroleum-Isostasy Model for Bearing Basin. Global Geol. 2003;22(4):319–25 **(in Chinese)**.

Liu RH, Jiang ZX, Wang M, et al. Reservoir characteristics and controlling factors of silurian lower Kepingtage Formation in Tahe Area, Tarim Basin, NW China. J Earth Sci. 2017;28(6):1135–44. https://doi.org/10.1007/s12583-016-0941-8.

Meng XJ, Zhang XH, Liu Z, et al. The basement structural characteristics of the North Xihu Sag in the East China Sea. Mar Geol Quat Geol. 2008;28(2):61–4 **(in Chinese)**.

Nie FJ, Jiang MZ, Wu KQ, et al. Tectono-magmatism and hot fluid flow in the Pearl River Mouth Basin South China Sea. J East China Inst Technol. 2005;28(2):107–11. https://doi.org/10.3969/j.issn.1674-3504.2005.02.002 **(in Chinese)**.

Oelkers EH, Schott J. Experimental study of anorthite dissolution and the relative mechanism of feldspar hydrolysis. Geochim Cosmochim Acta. 1995;59(24):5039–53. https://doi.org/10.1016/0016-7037(95)00326-6.

Schmidt K, Garbe-Schönberg D, Koschinsky A, et al. Fluid elemental and stable isotope composition of the Nibelungen hydrothermal field (8°18′ S, Mid-Atlantic Ridge): constraints on fluid–rock interaction in heterogeneous lithosphere. Chem Geol. 2011;280(2):1–18. https://doi.org/10.1016/j.chemgeo.2010.07.008.

Shen RQ, Li SQ, Xie RH. Magmatic activity of the East China Sea. Beijing: Geology Publishing House; 2001. p. 60–9 **(in Chinese)**.

Shu LS, Mu YF, Wang BC. The oil-gas-bearing strata and the structural features in the Songliao Basin, NE China. J Stratigr. 2003;27(4):340–7. https://doi.org/10.1016/S0955-2219(02)00073-0 **(in Chinese)**.

Su A, Chen HH, Wang GW, et al. Densification mechanism and diagenesis fluid evolution of low-porosity and low-permeability tight sandstone reservoirs: an example from the Huagang formation in the north of the central anticlinal zone in the Xihu depression, East China Sea. J China Univ Mining Technol. 2016;45(5):843–52. https://doi.org/10.13247/j.cnki.jcumt.000468 **(in Chinese)**.

Sugisaki R, Mimura K. Mantle hydrocarbons: abiotic or biotic? Geochim Cosmochim Acta. 1994;58(11):2527–42. https://doi.org/10.1016/0016-7037(94)90029-9.

Tao HX, Xu YX. Hydrothermal activity and oil–gas reservoirs. Pet Explor Dev. 1994;21(6):92–7 **(in Chinese)**.

Wang DR, Zhang YH. A Study of the origin of the carbonate cements within reservoirs in the external metamorphic belt of the Bohai Bay oil–gas bearing region. Pet Explor Dev. 2001;28(2):40–2 **(in Chinese)**.

Wang PJ, Chen SM, Li WZ, et al. Chronology, petrology and geochemistry of the Cretaceous crypto-explosive breccia-bearing volcanic rocks: implications for volcanic reservoir and tectonic of the Songliao Basin, NE China. Acta Pet Sin. 2010;26(1):33–46 **(in Chinese)**.

Wang XY, Wang XL, Hu WX, et al. Supercritical CO_2-involved water-rock interaction at 85°C and partial pressures of 10–20 MPa: sequestration and enhanced oil recovery. J Energy Explor Dev. 2017a;35(2):237–58. https://doi.org/10.1177/0144598716687933.

Wang YS, Liang C, Sun XN. Shale oil reservoir characteristics and enrichment in the Jiyang Depression, Bohai Bay Basin, East China. J Earth Sci. 2017b;28(6):977–86. https://doi.org/10.1007/s12583-016-0940-9.

Wang YX, Fan P, Cheng XH, et al. Influence of diabase intrusions on hydrocarbon generation of depositional organic matter. Oil Gas Geol. 1990;11(1):73–7 **(in Chinese)**.

Wei DW, Wu HL, Xu WL, et al. Evolution of the East China Sea Basin and its deep source heat. In: Proceedings of the tenth annual conference of the Chinese geophysical society. Beijing: Seismological Press; 1994. p. 186–87 (in Chinese).

Wierzbicki R, Dravis JJ, Al-Aasm I, et al. Burial dolomitization and dissolution of upper Jurassic Abenaki platform carbonates, deep Panuke reservoir, Nova Scotia, Canada. AAPG Bull. 2006;90(11):1843–61. https://doi.org/10.1306/03200605074.

Xu DY, Liu YQ, Zhang XH. China offshore geology. Beijing: Geological Publishing House; 1997. p. 12–8 **(in Chinese)**.

Yang WD, Wang ZY, Zeng JL. Geologic features of the Okinawa trough axis. Mar Geol Quat Geol. 2001;21(2):1–6 **(in Chinese)**.

Ye JR, Gu HR, Jia JY. Research into the hydrocarbon accumulation dynamics of the Xihu Sag, East China Sea Shelf Basin. Geol Explor. 2005;25(12):5–8 **(in Chinese)**.

Yu ZC, Liu L, Sun XM, et al. Evidence of paleogene thermal fluid activities and their impact on porosity-permeability of reservoirs in the Qikou Sag. J Jilin Univ (Earth Sci Ed). 2012;42(Sup. 3):1–13 **(in Chinese)**.

Zhang JP. Fault systems and their genetic mechanism in the Pinghu slope of the Xihu sag in the East China Sea shelf basin. Chin J Geol. 2013;48(1):291–303. https://doi.org/10.3969/j.issn.0563-5020.2013.01.020 **(in Chinese)**.

Zhang SL, Zhang JP, Tang XJ, et al. Geometry characteristics of the fault system in the Xihu Sag in the East China Sea and its formation mechanisms. Mar Geol Quat Geol. 2014;34(1):87–94. https://doi.org/10.3724/SP.J.1140.2014.01087 **(in Chinese)**.

Zhang YW, Zeng JH, Zhang SW, et al. An overview of feldspar dissolution experiments. Geol Sci Technol Inf. 2009;28(1):31–7. https://doi.org/10.3969/j.issn.1000-7849.2009.01.005 **(in Chinese)**.

Zhao GL. Study of petrological characteristics and thermodynamic mechanism of secondary pores in deep reservoirs, Songliao Basin. Beijing: China University of Geosciences; 2005 **(in Chinese)**.

Zhou XJ, Song ZC. Analysis of the prototype basin of the Xihu sag in Donghai. Wuxi: Wuxi Petroleum Geology Research Institute; 2014 **(in Chinese)**.

Zhou J. Thermal evolution of source rocks under two thermal systems in the central anticlinal zone in the Xihu sag, East China Sea Basin. China Offshore Oil Gas (Geology). 2003;17(1):64–8 **(in Chinese)**.

Zhu JX, Li SZ, Sun XM, et al. Discovery of early tertiary hydrothermal activity and its significance in oil/gas geology, Dongpu Depression, Henan Province, China. Chin J Geochem. 1994;13(3):270–81. https://doi.org/10.1007/BF02840333 **(in Chinese)**.